# Changing Vibration Coupling Strengths of Liquid Acetonitrile with an Angle-tuned Etalon

Justin D. Erwin, Ying Wang, Rebecca C. Bradley, James V. Coe*

Department of Chemistry and Biochemistry, The Ohio State University, Columbus OH 43210-1173, USA

E-mail coe.1@osu.edu

**Keywords:** Cavity-vibration polaritons, vibration-vibration coupling, Fabry-Perot cavities, etalons, Rabi splittings, Hopfield coefficients, complex index of refraction of liquids, interacting liquid acetonitrile vibrations

**Abstract**

This work is the first report on nonzero molecular vibration-vibration coupling in an infrared cavity-vibration experiment. Vibration-vibration coupling strength is determined as a cavity mode of parallel spaced mirrors (etalon mode or fringe) is angled-tuned in the region between two vibrations of liquid acetonitrile which are Fermi-coupled, namely a CN stretch dominated vibration and a nearby combination band dominated by the symmetric $CH_3$ bend and C-C stretch. All other infrared cavity-vibration work to date involving more than one vibration has used a value of zero for vibration-vibration coupling, however this work starts with Fermi-coupled vibrations and reveals that there are changes in the vibration-vibration coupling and cavity-vibration couplings as the cavity mode is angle-tuned between the interacting vibrations. The ability to change fundamental vibrational dynamics within a cavity is an exciting result which helps to build a foundation for understanding molecular vibrational dynamics in parallel plate etalon cavities.

## 1 Introduction

Cavity-vibration polaritons (also known as dressed states, hybrid states, or molecular polaritons) are mixed states of infrared cavity modes and vibrations of matter that can alter the chemical dynamics and reactivity[1-5] of ordinary matter. This work adds the effects of the Fermi coupling between two molecular vibrations to the coupling between each vibration and etalon cavity modes. Both processes contribute to the observed mixed states and change as a cavity mode is angle-tuned between the vibrations. There are many analogous mixed states including surface plasmon polaritons[6] and quantum wells[7] interacting with matter that inform work on molecules in solution. Ideas for collective molecular mixed states[8-9] and alterations in condensed phase chemical reactivity[10] ultimately arose from Nobel Prize-winning work on the dressed or mixed states of atoms in optical cavities[11-12]. Since initial work on cavity-vibration mixed states[13-16], there have been many measurements of collective"Rabi splittings" of strongly coupled vibrations of many condensed phase molecules in infrared parallel plate cavities (etalons or Fabry-Pérot cavities)[17-45]. To be more specific, Rabi splittings have been modeled to determine cavity-vibration coupling strength, but this work is differentiated by simultaneously getting vibration-vibration and cavity-vibration couplings which change as the etalon is angle-tuned. Considering that vibrational dynamics may play a role in the changed rates of chemical reactions performed inside of an etalon[1, 5, 24, 46-49], this work examines the fundamental aspects of varying both vibrational-vibration and vibration-cavity coupling dynamics with etalons.

The acetonitrile $\upsilon_2$ $C \equiv N$ stretch and $\upsilon_{3+4}$ combination band (symmetric $CH_3$ bend and C-C stretch)[50-51] have the same $A_1$ symmetry and interact by Fermi resonance. In liquid acetonitrile they interact to produce a peak with 60% $C \equiv N$ stretch character at 2253 $cm^{-1}$ and another with 60% combination band character at 2293 $cm^{-1}$. The vibrations without the Fermi resonance will

be referred to as the pre-Fermi basis and with the Fermi resonance as the post-Fermi basis. These observed bands of acetonitrile are well known to change frequency (spectral position in wavenumbers) upon interaction with different solvents[52-53] or metal cations[54] providing extensive evidence that these bands interact differently in different chemical environments. The observed frequencies (in wavenumbers) in liquid acetonitrile (2253 and 2293 $cm^{-1}$) arise primarily from an anharmonically coupled Fermi resonance[52] between the pre-Fermi $\upsilon_2$ CN stretch and pre-Fermi $\upsilon_{3+4}$ combination band with a $\beta$ coupling[55] of 19.6 $cm^{-1}$; so one can estimate that the pre-Fermi spectral positions would be 2269 and 2277 $cm^{-1}$ for the $\upsilon_2$ and $\upsilon_{3+4}$ bands, respectively. This work is analyzed in a post-Fermi basis because the observed transmission spectra show strong absorption within the cavity at the post-Fermi frequencies. Mixed transmission states can be obscured when they are too close to to the strong absorptions of the post-Fermi absorptions at 2253 and 2293 $cm^{-1}$, so the present model analysis is confined to tuning an etalon cavity mode from 2253 to 2293 $cm^{-1}$ in which three mixed states of high vibrational content are observed. Outside of this range, only two mixed states of high vibrational content are observed and it is not possible to determine vibrational-vibrational coupling.

An overall outline of this paper starts with the Experimental section which explains how the etalon was created and the conditions under which Fourier transform infrared (FTIR) transmission spectra of an etalon filled with liquid acetonitrile were recorded as a function of the etalon angle to the incident beam. The wavenumber positions and widths of transmission maxima are extracted by least squares fitting yielding experimental results for the cavity-vibration polaritons (mixed states) at each angle. Then, the Results section starts by describing transfer matrix (TM) method calculations of the etalon's transmission vs angle requiring the complex index of refraction $[\boldsymbol{N} = n(\tilde{\nu}) + ik(\tilde{\nu})]$ of liquid acetonitrile. $\boldsymbol{N}$ is expressed in terms

of the vibrations of liquid acetonitrile and the results are computed with and without the post-Fermi vibrations at 2253 and 2293 $cm^{-1}$ which we refer throughout as "target vibrations". Since the TM method model with all vibrations does a good job of predicting the energies or wavenumber spectral positions of the cavity-vibration polaritons, the critical feature is running the TM model without the selected target vibrations which predicts the presence of a cavity mode in the absence of interaction with the target vibrations. Consequently, the phrase "target vibrations" technically refers to vibrations left out of the TM simulation predicting transmission maxima, but in this work the "target vibrations" are distinctively chosen to have a strong Fermi interaction with each other outside of a cavity. Finally, the accurate wavenumber positions for the cavity modes before interaction with the target vibrations are used as basis functions in an interaction Hamiltonian matrix analysis. The target vibrations are generalized and called Vibration 1 (vib1) and Vibration 2 (vib2) in the Hamiltonian. Coupling parameters for vibration-vibration and vibration-cavity interactions are varied until the eigenvalues of this interaction Hamiltonian are optimally in agreement with the measured cavity-vibration polaritons. The ultimate results show that both the cavity-vibration and vibration-vibration coupling constants vary as a cavity mode is tuned between the target vibrations.

## 2 Experimental

The experiments proceed by recording Fourier transform infrared (FTIR) transmission spectra of an etalon filled with liquid acetonitrile as a function of incident angle, $\theta$. Etalon mirrors are created by coating the standard ZnSe windows of a commercial Harrick liquid cell (DLC-S13) with a gold coating. ZnSe optical windows (13 mm x 2 mm ZnSe circular, Crystran Ltd.) were coated by E-gun evaporation (Denton 502A Evaporator) at the Ohio State University Nanotech West Lab with a 2 nm Ti attachment layer and 10 nm of Au. These mirrors are reinserted into

the empty Harrick liquid cell with a polytetrafluoroethylene (PTFE, Harrick MSP-056-M13) spacer of nominally 56 μm and the cavity filled with acetonitrile (Pharmco, 99.5%, #PL000T). The angle of the cell with respect to light was changed with an Edmund Optics rotary mount (#53-026) at the following angles $\theta = 0, 1, 2, 3, \ldots 20^0$, where 0 is perpendicular incidence, and then in a subsequent experiment, $\theta = 0, -1, -2, -3, \ldots -20^0$. Transmission spectra were recorded at each angle [Perkin Elmer Spectrum 100 FTIR, 4 $cm^{-1}$ resolution, $N_2(\ell)$-cooled mercury-cadmium-tellurium (MCT) detector, 2 $cm^{-1}$ steps, 600-6000 $cm^{-1}$ range, 128 scans]. A contour diagram of the transmission of the positive $\theta$ results in momentum space is shown in Figure 1. Note that $k_x = 2\pi\tilde{\nu}sin\theta$, where $\theta$ is the angle of the etalon to the incident beam and

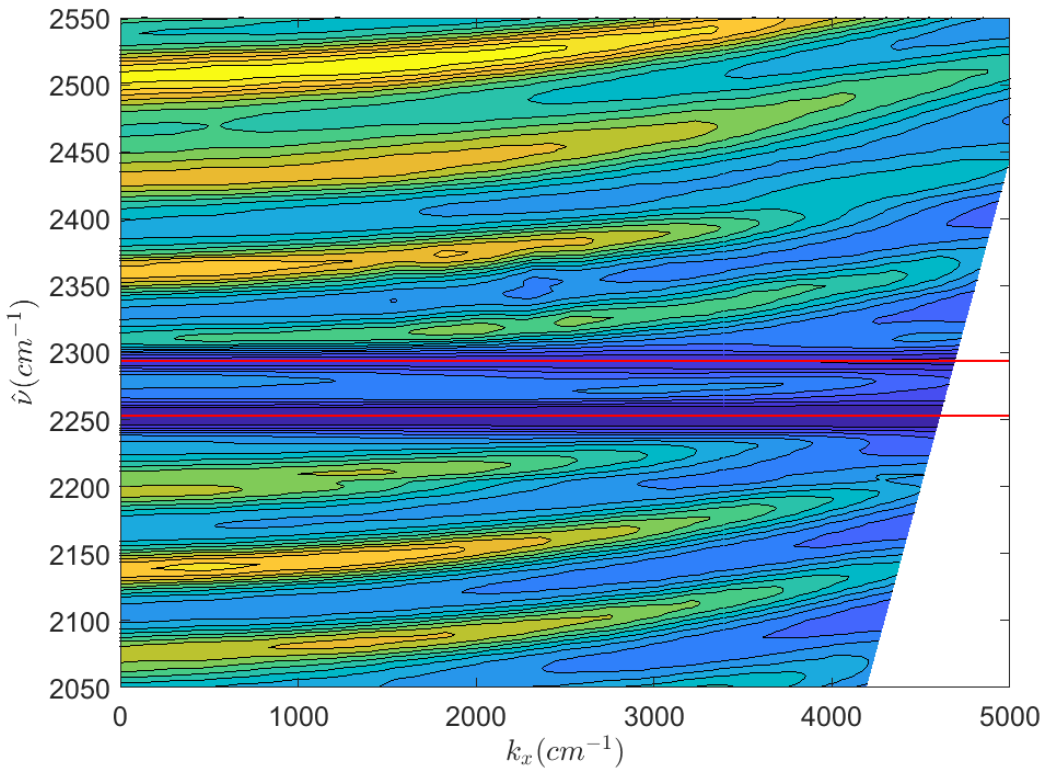


Figure 1. Contour dispersion plot of transmittance measurements of liquid acetonitrile in the CN stretching region with a nominally 56 μm etalon spacer, at $\theta$ values from 0 to 20°, where $k_x = 2\pi\tilde{\nu}sin\theta$ Strong absorption features of the target vibrations at 2253 and 2293 $cm^{-1}$ are shown with red lines. High transmission is given in yellow and low transmission in dark blue. Cavity modes have quadratic dispersion unless interrupted by vibration interactions.

the target vibrations are indicated with red horizontal lines. The spacing between the mirrors, $d$, was nominally 56 μm, but the TM method simulations, to be described in following sections, determined values in the vicinity of of 50.800 μm. The exact value of $d$ drifts with temperature changes in the room and by FTIR irradiation, so the exact value varied and was determined at each different angle of the data by matching the TM simulation to experiment. Note that etalons operating in the midinfrared have modes with increasing width and intensity[56] upon increasing wavenumber. The TM simulation captures this feature and is the key to pinning down the changing finesse, free spectral range, and behavior of the etalon.

## 3 Results

The wavenumber positions and widths of the experimental cavity-vibration polaritons are determined in Section 3.1, while the experimental complex index of refraction of liquid acetonitrile is converted into a function of vibrations in Section 3.2. Then, the featured method of fringe reconstruction by the TM simulations is presented in Section 3.3 determining the wavenumber position of cavity modes before interaction with the target vibrations. The model Hamiltonian yields eigenvalues of the wavenumber positions of the cavity-vibration polaritons which are optimized by varying vibration-vibration and cavity-vibration coupling parameters as shown in Section 3.4. Finally, Section 3.5 investigates the cavity-vibration mixtures and Section 3.6 addresses issues with our interaction Hamiltonian.

**3.1 Mixed State Fits.** The measured transmittance data are shown in Figure 2 at $\theta = 0^0$, using filled symbols as an example at one angle. Considering that etalon cavity modes are transmission maxima, it is useful to note that the cavity-vibration polaritons manifest here as transmission maxima. In fact, nine transmission maxima are observed in Figure 2 and fit to

Lorentzians. In contrast, the absorption of strong molecular vibrations leads to a wipeout of infrared light or transmission minimum at the vibrational band center and two such features are indicated with green arrows in Figure 2, namely the $\upsilon_2$ and $\upsilon_{3+4}$ dominated absorptions at 2253 and 2293 cm$^{-1}$ our target vibrations. These absorption features do not obey Beer's Law because the experiment is conducted within an etalon. The absorption features are fit with negative Lorentzians constrained to the positions and widths (in wavenumbers) of Table 1. The nine transmission maxima and two absorption features were simultaneously fit[57] using Matlab's "NonLinearModel.fit" function which required very close initial guesses due to sensitive regions of overlap between transmission states and vibrational absorption. The resulting fit is shown with a solid curve in Figure 2 and the wavenumber positions (black labels) and full-widths-at-half-maxima (blue labels) of all features are given as labels in Figure 2, complete with fitted

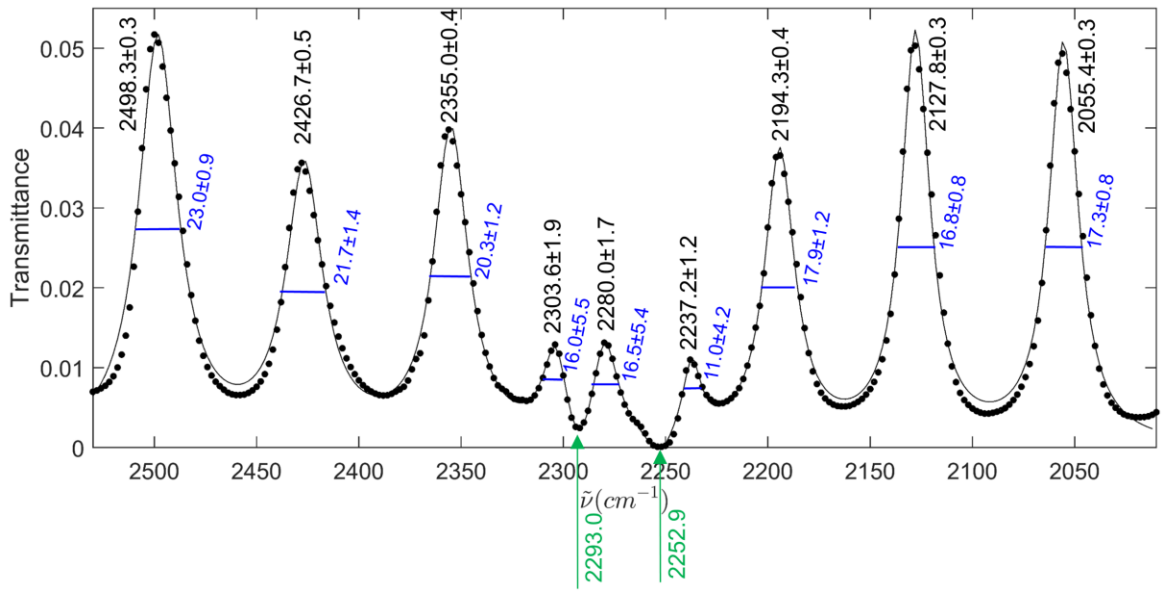


Figure 2. FTIR transmittance measurement of liquid acetonitrile in the CN stretching region with a nominally 56 μm etalon spacer (filled symbols) at $\theta$=0$^0$. A multiple nonlinear regression fit was performed (solid curve) with a linear combination of Lorentzian functions of nine transmission maxima (up-going) and two vibrational, down-going, absorption features at 2253 and 2293 cm$^{-1}$ (green arrows). The fitted wavenumber positions and widths of the mixed states are given as labels with uncertainties.

uncertainties. Fits of this sort were performed at all of the angles in which a central cavity mode would have fallen between the vibrations - in the absence of the target vibrations.

The quantitative task of the following section is to determine how the spectrum in Figure 2 would appear if there were not two strong, interacting vibrations in the center. Qualitatively without vibrations, there would have been a cavity mode in the center of Figure 2. Instead, there is an interaction of that expected cavity mode with the two target vibrations leading to the primary observation of three less intense transmission maxima in the center of Figure 2. It will be shown later in Section 3.5 that the six strongest transmission features toward the outside of Figure 2 have high fractional contributions from cavity modes. While the six strongest transmission features are dominated by cavity modes, they actually occur at locations shifted from their spectral positions in the absence of target vibrations. This will be important in understanding the interaction Hamiltonian. Likewise, the three smaller transmission maxima towards the center of Figure 2 are cavity-vibration states with high vibrational character. They arise from the primary interaction of one primary cavity mode (the central fringe) and the two target vibrations. If this was all that was important, then only a 3x3 internal Hamiltonian model would be needed. So, it is useful to keep in mind that all of these measured transmission maxima are cavity-vibration mixed states. They will be modeled as the eigenvalues of our interaction Hamiltonian which should be distinguished from the basis set inputs which are the energetic locations of the states before interaction. All of this depends on being able to remove the effect of the target vibrations which is the subject of the next section.

**3.2 Optical Constants of Acetonitrile with Vibrational Resonances**. The best literature complex index of refraction, $\boldsymbol{N}$, of acetontrile has a digital form[58] and it has been fit to an analytical form as the square root of a sum of Lorentz oscillators (damped harmonic oscillators)[59]

$$\boldsymbol{N} = n(\tilde{\nu}) + ik(\tilde{\nu}) = \sqrt{\varepsilon_0 + \sum_j \frac{A_j \tilde{\nu}_{0,j}^2}{\tilde{\nu}_{0,j}^2 - \tilde{\nu}^2 - i\Gamma_j \tilde{\nu}}} \quad , \qquad (1)$$

where $\varepsilon_0$ is a high wavenumber value fixed at $1.3340^2$=1.7796 for acetonitrile, $A_j$ is a unitless measure of transition strength of vibration $j$, $\tilde{\nu}_{0,j}$ is the vibrational peak position in wavenumbers, and $\Gamma_j$ is the full-width-at-half-maximum of the vibration in wavenumbers. With the complex index of refraction expressed in terms of vibrations, it becomes possible to predict the transmission spectrum without the effect of target vibrations. The best TM simulation of the experimental fit is recalculated without the target vibrations (post-Fermi $\upsilon_2$ and $\upsilon_{3+4}$ dominated vibrations) providing an accurate prediction of etalon fringe maxima without an interaction with the target vibrations.

An accurate, frequency-dependent, complex index of refraction throughout the infrared region is required and available for acetonitrile. Using the methods of Bertie and coworkers[60-63] (FTIR measurements with different spacers and using multiple anchor points to enforce Kramers-Kronig relationships), a group at the Pacific Northwest National Laboratory (PNNL) reports a large and accurate library of the complex index of refraction of many liquids[58] including acetonitrile. The Nelder-Mead simplex algorithm[64-66] requiring no derivatives was used by means of Matlab's "fminsearch" function to fit the literature index of refraction to Equation (1) using 69 optimized vibrational terms or 207 variables. The optimized set of $A_j$, $\tilde{\nu}_{0,j}$, and $\Gamma_j$ parameters were determined by minimizing the difference of the Equation 1 predictions and the PNNL group's $n(\tilde{\nu})$ and $k(\tilde{\nu})$ values by the figure of merit, $\sigma_n + \sigma_k$, where $\sigma_n$ and $\sigma_k$ are the standard deviation of comparison to the PNNL experimental values. The fit was good to 0.0002 in both $n(\tilde{\nu})$ and $k(\tilde{\nu})$ and the optimized parameters are given in Table 1 and produce the red traces in Figure 3. Note that the target vibrations (post-Fermi $\upsilon_2$ $C \equiv N$ stretch

dominated and the $\upsilon_{3+4}$ combination band dominated) are the entries at $j = 15, 16$, respectively. Consider the following list of three issues: this process assumed Lorentzian lineshapes (whereas some vibrational lineshapes have small Fano-like distortions[67] from Lorentzian), the very wide vibrations likely correspond to sets of many unresolved sets of actual levels, and small vibrations in the wings of strong vibrations may not be fit. So the fit to Equation (1) is not as accurate as the original PNNL data, but more than sufficient for the present purposes. Most importantly, this analytical form allows vibrational peaks to be removed for the strategy of reconstructing fringes as shown by the blue traces in Figure 3.

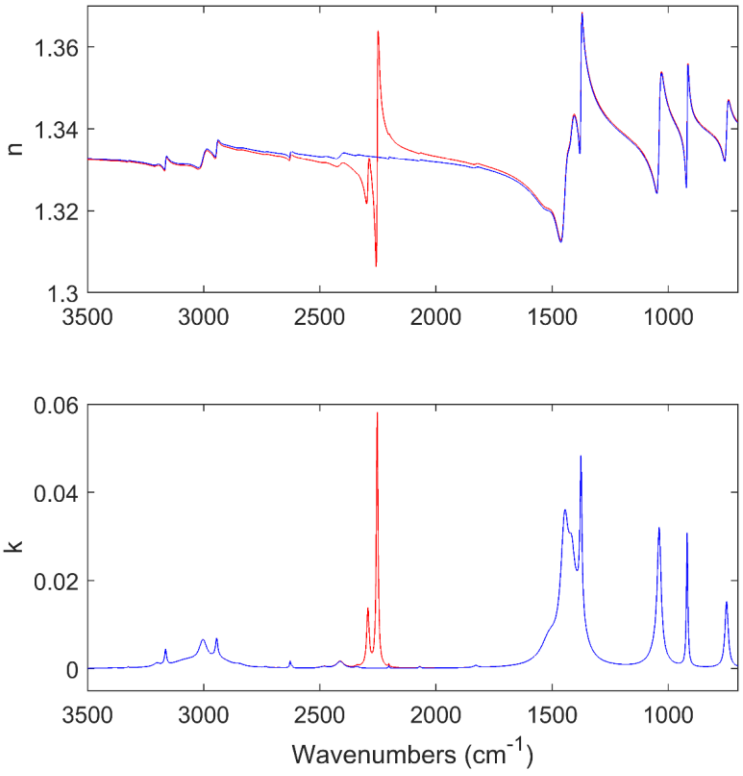


Figure 3. Complex index of refraction of liquid acetonitrile with (red) and without (blue) the two target vibrations which are dominated by $\upsilon_2$ and $\upsilon_{3+4}$.

**Table 1.** Damped harmonic oscillator parameters for the complex index of refraction of acetonitrile liquid with $\varepsilon_0$= 1.3340[2]. *The first peak is not an actual vibration.

| $j$ | $A_j$ | $\tilde{\nu}_{0,j}$ (cm$^{-1}$) | $\Gamma_j$ (cm$^{-1}$) | $j$ | $A_j$ | $\tilde{\nu}_{0,j}$ (cm$^{-1}$) | $\Gamma_j$ (cm$^{-1}$) |
|---|---|---|---|---|---|---|---|
| 1 | 1.485E-03* | 419.05* | 84.48* | 36 | 6.667E-07 | 3547.31 | 17.70 |
| 2 | 2.961E-05 | 659.93 | 15.48 | 37 | 1.313E-06 | 3617.45 | 10.75 |
| 3 | 8.990E-04 | 748.74 | 16.67 | 38 | 2.842E-06 | 3655.46 | 22.40 |
| 4 | 6.241E-04 | 918.39 | 7.05 | 39 | 3.907E-06 | 3927.49 | 47.20 |
| 5 | 1.429E-03 | 1038.77 | 19.47 | 40 | 5.314E-06 | 3975.33 | 22.22 |
| 6 | 6.223E-04 | 1051.86 | 65.55 | 41 | 9.114E-06 | 4029.27 | 24.96 |
| 7 | 6.312E-04 | 1375.58 | 9.53 | 42 | 4.103E-06 | 4080.81 | 42.15 |
| 8 | 1.329E-03 | 1386.31 | 63.43 | 43 | 4.045E-06 | 4321.81 | 15.93 |
| 9 | 9.648E-04 | 1416.14 | 35.08 | 44 | 1.230E-05 | 4362.47 | 21.40 |
| 10 | 2.055E-03 | 1445.69 | 40.14 | 45 | 1.884E-06 | 4374.17 | 20.23 |
| 11 | 7.940E-04 | 1512.66 | 85.74 | 46 | 1.110E-05 | 4394.62 | 24.21 |
| 12 | 1.524E-05 | 1827.77 | 21.88 | 47 | 1.589E-05 | 4439.20 | 25.94 |
| 13 | 4.248E-06 | 2069.24 | 9.58 | 48 | 2.598E-06 | 4473.12 | 19.68 |
| 14 | 3.459E-06 | 2202.98 | 4.54 | 49 | 5.149E-07 | 4983.94 | 21.79 |
| 15 | 5.771E-04 | 2252.94 | 8.37 | 50 | 3.953E-07 | 5079.60 | 26.37 |
| 16 | 1.886E-04 | 2292.96 | 12.45 | 51 | 4.899E-07 | 5133.27 | 55.06 |
| 17 | 6.667E-06 | 2339.69 | 17.71 | 52 | 8.023E-07 | 5194.09 | 20.10 |
| 18 | 6.345E-05 | 2412.19 | 37.22 | 53 | 1.983E-07 | 5204.32 | 28.69 |
| 19 | 1.166E-05 | 2481.13 | 32.81 | 54 | 4.226E-07 | 5353.31 | 42.48 |
| 20 | 5.872E-07 | 2500.70 | 15.22 | 55 | 2.245E-07 | 5408.19 | 28.96 |
| 21 | 2.030E-06 | 2620.25 | 5.43 | 56 | 2.631E-07 | 5678.26 | 17.98 |
| 22 | 9.803E-06 | 2627.80 | 6.22 | 57 | 4.112E-07 | 5719.26 | 28.19 |
| 23 | 5.838E-07 | 2674.78 | 10.59 | 58 | 4.556E-06 | 5824.72 | 57.02 |
| 24 | 2.612E-06 | 2732.24 | 15.10 | 59 | 1.037E-08 | 5889.82 | 30.12 |
| 25 | 1.238E-05 | 2843.47 | 38.04 | 60 | 1.998E-06 | 5953.77 | 25.47 |
| 26 | 2.104E-04 | 2936.93 | 124.71 | 61 | 3.314E-07 | 6001.00 | 20.96 |
| 27 | 4.624E-05 | 2944.40 | 12.17 | 62 | 9.547E-08 | 6471.74 | 52.20 |
| 28 | 1.646E-07 | 2958.25 | 11.55 | 62 | 8.798E-08 | 6568.75 | 73.71 |
| 29 | 1.708E-04 | 3003.49 | 39.34 | 64 | 1.453E-07 | 6813.87 | 30.48 |
| 30 | 2.022E-04 | 3075.32 | 147.85 | 65 | 1.531E-07 | 6845.46 | 70.03 |
| 31 | 2.885E-05 | 3164.36 | 9.86 | 66 | 5.293E-08 | 6944.33 | 19.63 |
| 32 | 2.249E-06 | 3198.96 | 36.69 | 67 | 2.859E-07 | 7078.32 | 80.99 |
| 33 | 1.657E-05 | 3201.95 | 31.20 | 68 | 7.815E-08 | 7703.93 | 37.47 |
| 34 | 1.053E-06 | 3324.61 | 5.89 | 69 | 5.783E-08 | 8390.37 | 62.41 |
| 35 | 1.817E-06 | 3384.66 | 26.67 | | | | |

**3.3 Fringe Reconstruction with Experimental Comparison.** The experimental transmission data were modeled with the TM method[68] which propagates the electric and magnetic fields of light through smooth layers of lossy material of fixed thickness as a function of incident angle, i.e. a mirror/acetonitrile/mirror system. This approach has been applied for vibrations interacting with one fringe[15-16, 20, 28], but this is the first paper including interaction with any subset of the

vibrations and multiple fringes, i.e. seven in this work. The essential feature is a matching of the electric and magnetic fields at the interface between two materials. The program outputs the complex reflectance and transmission coefficients, as well as the fraction of light transmitted, reflected, and absorbed by the system. Our implementation follows that of Pascoe[69] regarding equations and Matlab coding. Our program is given in the supplementary materials, uses an unpublished Matlab function called "jreftran_rt.m" from the work of Shawn Divitt (ETH Zurich Photonics Group, 2016), and our primary contribution is adapting to the midinfrared range. The program used a complex index of refraction from Equation 1 with Table 1 data for liquid acetonitrile, as well as a 2.0 nm layer of Ti on ZnSe and a 3.8 nm layer of gold on the Ti for the mirrors where the metal permittivity came from the Lorentz-Drude model of Rakic et al[70]. Since, the TM program does not account for instrumental spectral resolution or angular spread, the thickness of the gold layers was set artificially small to produce wider fringes that better matched experiment.

The thickness of the etalon spacer, $d$, in the TM program was varied until every measured transmission peak in the range from 600-6000 $cm^{-1}$ had only one corresponding simulation peak. This gave a unique value of $d$ which was more carefully adjusted (about 50.800 μm in this case) to give a good simulation of the transmission peaks in the vicinity of the target vibrations (compare the green trace to the black symbols in Figure 4). The only difference between the green and blue curves in Figure 4 is that the target vibrations at 2253 $cm^{-1}$ and 2293 $cm^{-1}$ were removed [had their intensities ($A_{15}$ and $A_{16}$ in Table 1) multiplied by zero] so that the blue trace in Figure 4 predicts the spectral position of cavity modes in the absence of the target vibrations, but including the effect of all of the other vibrations. The blue and green traces were scaled by the same factor which was chosen to make the green curve similar to experiment. The

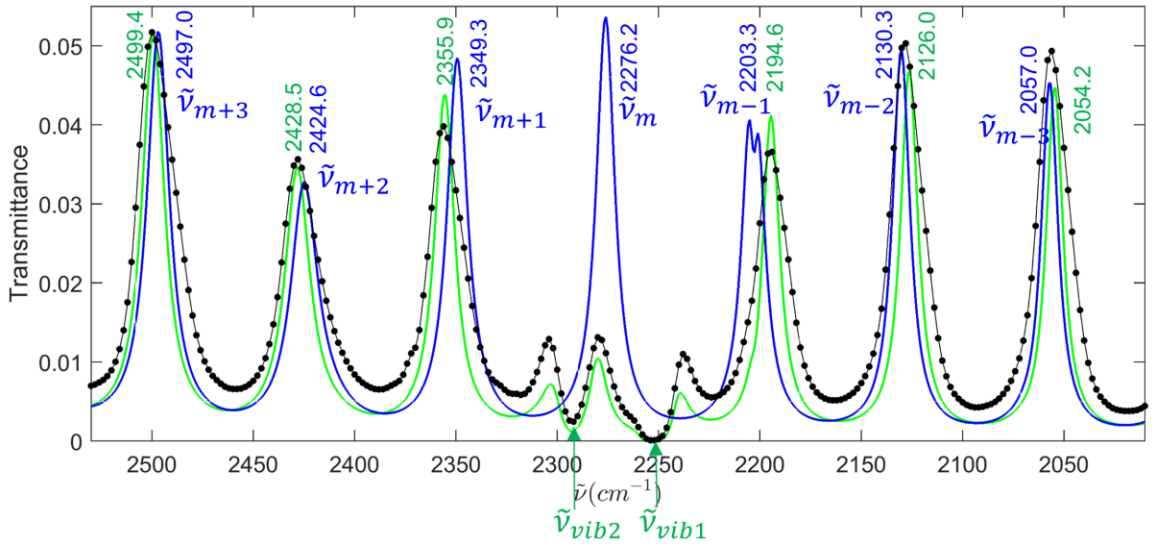


Figure 4. TM predictions in the acetonitrile $C \equiv N$ stretching region with (green) and without (blue) the vibrations at 2253 cm$^{-1}$ and 2293 cm$^{-1}$ at the cavity tilt angle of $\theta$=0°. The simulation without target vibrations (green) was adjusted to model the experimental wavenumber positions (black symbols). Both TM predictions were scaled by the same factor to provide a good overlay. Without the vibrations, there would be a strong fringe at 2276.2 cm$^{-1}$ which interacts strongly with the vibrations at 2253 cm$^{-1}$ and 2293 cm$^{-1}$. The transmission maxima spectral positions of the blue trace were determined by least square fits to Lorentzians.

TM program provides useful relative intensities between the blue and green curves and a wavenumber accuracy of better than 1 cm$^{-1}$ in this region. The primary result is that without vibrations at 2253 and 2293 cm$^{-1}$, there would have been a strong cavity mode at 2276.2 cm$^{-1}$. Interaction of the central cavity mode ($\tilde{\nu}_m$) with the two vibrations ($\tilde{\nu}_{vib1}$ and $\tilde{\nu}_{vib2}$) produces three highly mixed states of less transmission (2232, 2280, and 2304 cm$^{-1}$) at the center of Figure 2.

A nominally 56 μm spacer was chosen to get fringes with widths comparable to the vibrational widths[56] making observed splittings easier to interpret by simple models. An experimental estimate of the etalon free spectral range (spacing between adjacent etalon fringes) can be made by noticing 6 such spacings in the blue curve in Figure 4 which when considered with the experimental outer transmission positions of Figure 2 give an estimated free spectral

range of $73.82 \pm 0.07\ cm^{-1}$ without the target vibrations. Only 4 such spacing are apparent in Figure 2 and they give adjacent spacing varying from from 66-73 $cm^{-1}$, i.e. not constant. This illustrates the strong effect of the target vibrations on typical etalon behavior. The question arises as to how much the other etalon cavity modes are affected by vibrational interactions, so the cavity modes before target vibration interaction have been labelled as $\tilde{\nu}_{m-3}, \tilde{\nu}_{m-2}, \ldots, \tilde{\nu}_{m+3}$ in Figure 4 to facilitate this discussion. The primary interaction of the vibrations is with $\tilde{\nu}_m$, the primary etalon cavity mode, but the other fringes exhibit shifts (see the difference between the green and blue traces of Figure 4). Upon interaction the $\tilde{\nu}_{m-1}$, $\tilde{\nu}_{m-2}$, and $\tilde{\nu}_{m-3}$ fringes are shifted 8.7, 4.3, and 2.8 $cm^{-1}$ to lower wavenumber, while the $\tilde{\nu}_{m+1}$, $\tilde{\nu}_{m+2}$, and $\tilde{\nu}_{m+3}$ are shifted 6.6, 3.9, and 2.4 $cm^{-1}$ to higher wavenumber, i.e. each away from the primary interactions. The magnitude of the shifts gets smaller as the fringes occur further away in energy from the primary interaction. Consequently, all seven of the fringes before interaction in Figure 4 (blue trace) are detectably involved in the interaction with the two vibrations. So, the quantum mechanical (QM) interaction Hamiltonian model devised in this work for the cavity-vibration interaction involves seven fringes before interaction and two vibrations before placement in the cavity. It may useful for some to understand that these effects are correlated with the well-known change in index of refraction associated with molecular vibrational transitions. However, the question to be addressed is how much the addition of more fringes in the basis affects the eigenenergies and the value of the QM cavity-vibration and vibration-vibration coupling constants.

**3.4 Cavity-Vibration QM Interaction Hamiltonian.** There are now a number of theoretical papers on strong vibrational coupling[71-75], but they do not cover the issues in this work. A simple and approximate 9x9 cavity-vibration interaction Hamiltonian was constructed from a

quantum electrodynamic perspective[76-77] using the two acetonitrile target vibrations ($\tilde{\nu}_{vib1}$ and $\tilde{\nu}_{vib2}$) and the seven TM predicted cavity modes (etalon cavity mode positions in wavenumbers without the target vibrations) as

$$\mathbf{H} = \begin{bmatrix} \tilde{\nu}_{m-3} & 0 & 0 & 0 & 0 & 0 & 0 & V_1 & V_2 \\ 0 & \tilde{\nu}_{m-2} & 0 & 0 & 0 & 0 & 0 & V_1 & V_2 \\ 0 & 0 & \tilde{\nu}_{m-1} & 0 & 0 & 0 & 0 & V_1 & V_2 \\ 0 & 0 & 0 & \tilde{\nu}_{m} & 0 & 0 & 0 & V_1 & V_2 \\ 0 & 0 & 0 & 0 & \tilde{\nu}_{m+1} & 0 & 0 & V_1 & V_2 \\ 0 & 0 & 0 & 0 & 0 & \tilde{\nu}_{m+2} & 0 & V_1 & V_2 \\ 0 & 0 & 0 & 0 & 0 & 0 & \tilde{\nu}_{m+3} & V_1 & V_2 \\ V_1 & V_1 & V_1 & V_1 & V_1 & V_1 & V_1 & \tilde{\nu}_{vib1} & W \\ V_2 & V_2 & V_2 & V_2 & V_2 & V_2 & V_2 & W & \tilde{\nu}_{vib2} \end{bmatrix}, \quad (2)$$

where the diagonal contains $\tilde{\nu}_{m-3}, \tilde{\nu}_{m-2}, \ldots \tilde{\nu}_{m+3}$ for the seven cavity mode wavenumber positions before interaction (see Figure 4 in blue) and $\tilde{\nu}_{vib1}$ and $\tilde{\nu}_{vib2}$ which are the post-Fermi interaction vibrations of pure liquid acetonitrile (2252.9 and 2293.0 cm$^{-1}$ from Table 1). The vibration-vibration coupling, $W$, has been taken as zero in all other cavity-vibration work of which we are aware, however none of the previous studies included vibrations with strong Fermi interactions. Another aspect of this Hamiltonian is that each vibration has an equal coupling to each and every cavity mode enabling neighboring cavity modes to experience shifts as observed in the data (compare the green and blue curves in Figure 4).

The calculated eigenvalues, $E_{cal,i}$, of the Hamiltonian in Equation 2 are compared to the measured mixed state, $E_i$, in wavenumber units as might be extracted from Figure 2, to define the figure of merit as a standard deviation

$$\sigma = \sqrt{\sum_{i=1}^{n} \frac{(E_{cal,i} - E_i)^2}{n-3}}, \quad (3)$$

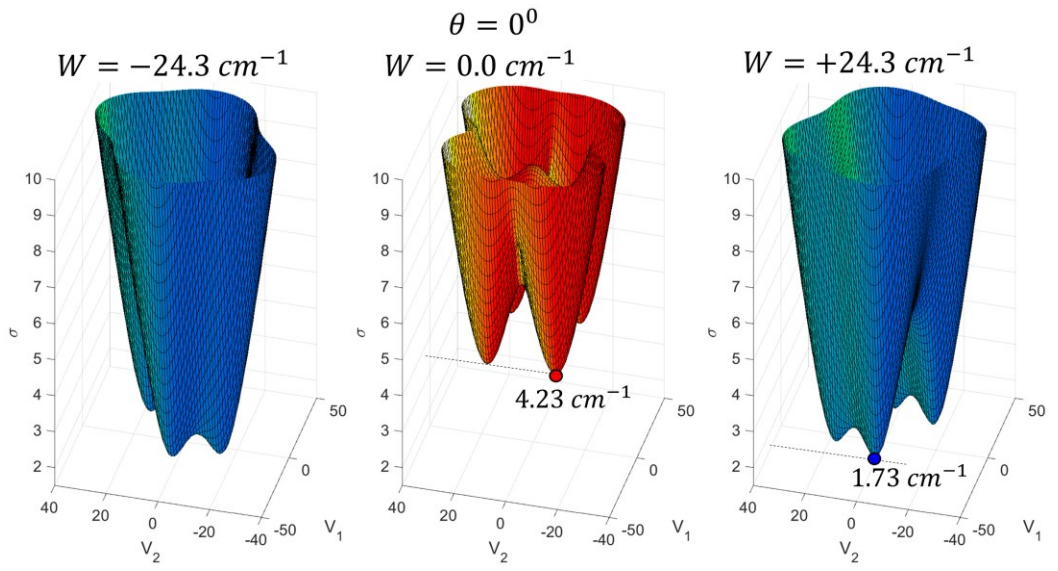


Figure 5. Standard deviation of comparison between eigenvalues and measured mixed states at $\theta = 0^0$ as a function of the vibration-vibration coupling parameter, $W$, which was fixed at selected values while both of the fringe-vibration coupling parameters were optimized. The optimized value of 4.23 $cm^{-1}$ is highest at $W$=0 $cm^{-1}$ as shown with a red symbol in the middle plot, while the optimized value of 1.73 $cm^{-1}$ is minimal at $W$=24.3 $cm^{-1}$ as shown with a blue symbol on the right hand side.

where $n = 9$ is the dimension of the Hamiltonian and three parameters were determined in the analysis, namely the coupling parameters, $V_1$, $V_2$, and $W$. The nature of the solutions was explored by calculating the figure of merit, $\sigma$ , over a gridded set of $V_1$, $V_2$, and $W$. Given four dimensional results, selections at three fixed values of $W$ are shown in Figure 5. At the incident angle of $\theta = 0^0$, the values of $\sigma$ as a function of $V_1$ and $V_2$, are shown at the optimized values of $W$ on the right and left sides of Figure 5. In general, there are eight minima for each magnitude of $W$, i.e. 4 minima for the positive value of $W$ on the right and 4 minima for the negative value on the left. The minima have the exact same value of $\sigma$ to all calculated figures. The eight values represent all of the sign permutations between the three coupling parameters and are fully tabulated in the supplementary materials. There are two different pairs of solutions for $V_1$, $V_2$ with different magnitudes and a smaller separating barrier for each non-zero absolute magnitude

of $W$. The result at the fixed value of $W = 0$ is shown at the center of Figure 5. When $W = 0\ cm^{-1}$ there is no vibration-vibration coupling and the value of $\sigma$ doubles and the pairs of two $V_1$, $V_2$ collapse into one as shown in the center of Figure 5. Given, the details about sign permutations and the paired solutions, $V_1$ and $V_2$ initial values of coupling parameters were chosen to find all eight optimized sets of the three parameters at each angle $\theta$ to minimize $\sigma$ by means of the Nelder-Mead[64-66] downhill simplex algorithm (Matlab's "fminsearch.m" function) until optimal agreement was obtained between $E_{cal,i}$ and $E_i$. The program for doing this is given in the supplementary material. After the couplings were optimized, a Hessian matrix was calculated numerically to estimate the uncertainties in the coupling parameters. These programs were run at each angle in the data set which gave a cavity mode (before interaction) between the two target vibrations. The unique results are listed in Table 2 and plotted in Figure 6. The results are color coded, there is

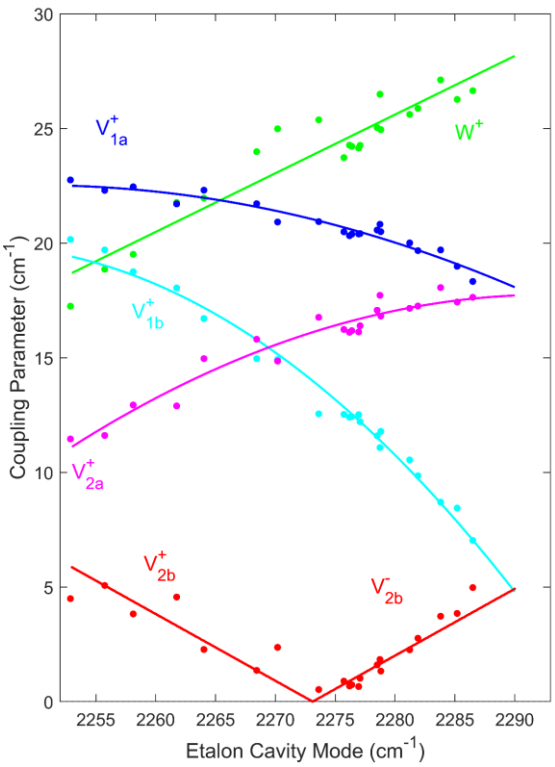


Figure 6. All-positive coupling strengths as the fringe position or primary cavity mode is tuned between the target vibrations of acetonitrile. The $V_1$ cavity-vibration coupling of the CN stretch dominated fundamental has two branches labelled as $V_{1a}^{+}$ (blue) and $V_{1b}^{+}$ (cyan). The $V_2$ cavity-vibration coupling of the combination band dominated vibration also has two branches labelled $V_{2a}^{+}$ (magenta) and $V_{2b}^{+}$ (red). There is a mirror image vertically about zero. The positive $W^{+}$ branch of vibration-vibration coupling is shown in green. These couplings change as shown with fitted solid lines as a function of the position of the primary fringe which was reconstructed by the TM method.

symmetry about the horizontal zero axis, and the two displayed branches of $V_1$ solutions are labelled as $V_{1a}^{+}$ (blue) and $V_{1b}^{+}$ (cyan) and those of $V_2$ are labelled $V_{2a}^{+}$ (magenta) and $V_{2b}^{+}$ (red). Each set has a negative equivalent of which the $V_{2b}^{-}$ (red) is seen at the lower right. Most interestingly, the $V_{1a}^{+}$ and $V_{2a}^{+}$ merge as the central cavity mode is tuned from 2253 to 2293 cm$^{-1}$, while similarly $V_{1b}^{+}$ and $V_{2b}^{-}$ merge over the same range. In other words, the fundamental couplings of vibration to cavity mode change in a systematic way as an etalon cavity mode is is tuned between the two target vibrations with a Fermi interaction.

**Table 2.** Coupling Constants vs Cavity Mode Position. Vib 1 occurs at 2252.9 cm$^{-1}$ and Vib 2 occurs at 2293.0 cm$^{-1}$ in the absence of a cavity. $V_1$ is the fringe coupling of the $\nu_2$ CN stretch dominated fundamental, $V_2$ is the fringe coupling of the $\nu_3 + \nu_4$combination dominated vibration, and $W$ is the all positive coupling between the fundamental and combination bands. The incident angle, $\theta$, was varied to tune the primary fringe position.

| Fringe Pos. (cm$^{-1}$) | $\theta$ (deg.) | $V_{1a}^{+}$ (cm$^{-1}$) | $V_{1b}^{+}$ (cm$^{-1}$) | $V_{2b}^{+}$ (cm$^{-1}$) | $V_{2a}^{+}$ (cm$^{-1}$) | $W^{+}$ (cm$^{-1}$) |
|---|---|---|---|---|---|---|
| 2252.9 | -7 | 22.7±2.7 | 20.2±4.0 | 4.5±7.9 | 11±8 | 17.2±3.1 |
| 2255.7 | -8 | 22.3±1.9 | 19.7±2.6 | 5.1±5.2 | 12±5 | 18.9±1.8 |
| 2258.1 | -9 | 22.5±1.4 | 18.7±1.8 | 3.8±3.4 | 12.9±3.2 | 19.5±1.6 |
| 2261.7 | -10 | 21.7±0.9 | 18.0±1.0 | 4.6±1.9 | 12.9±1.6 | 21.8±0.8 |
| 2264.0 | -11 | 22.3±0.6 | 16.7±0.7 | 2.3±1.2 | 15.0±1.0 | 22.0±0.8 |
| 2268.0 | -12 | 21.7±0.7 | 15.0±0.7 | 1.4±1.2 | 15.8±1.1 | 24.0±0.9 |
| 2270.2 | -13 | 20.9±2.5 | 14.9±2.5 | 2.4±4.1 | 15±4 | 25.0±2.6 |
| 2273.6 | -14 | 20.9±1.2 | 12.6±1.1 | -0.5±1.6 | 16.8±1.5 | 25.4±1.4 |
| 2275.7 | 3 | 20.5±1.9 | 12.5±1.7 | -0.9±2.4 | 16.2±2.3 | 23.7±2.4 |
| 2276.2 | 0 | 20.3±1.8 | 12.4±1.7 | -0.7±2.4 | 16.1±2.2 | 24.3±2.3 |
| 2276.4 | 1 | 20.4±1.8 | 12.4±1.7 | -0.7±2.4 | 16.2±2.2 | 24.2±2.3 |
| 2277.0 | 2 | 20.4±1.9 | 12.5±1.8 | -0.7±2.5 | 16.1±2.3 | 24.1±2.5 |
| 2277.1 | 4 | 20.4±1.7 | 12.2±1.6 | -1.0±2.2 | 16.4±2.1 | 24.3±2.2 |
| 2278.5 | 6 | 20.6±1.9 | 11.6±1.8 | -1.6±2.3 | 17.1±2.1 | 25.0±2.5 |
| 2278.7 | -15 | 20.8±1.4 | 11.1±1.3 | -1.8±1.7 | 17.7±1.5 | 26.5±1.8 |
| 2278.8 | 5 | 20.5±2.0 | 11.8±1.9 | -1.3±2.5 | 16.8±2.3 | 24.9±2.7 |
| 2281.2 | 7 | 20.0±1.8 | 10.5±1.7 | -2.3±2.1 | 17.1±2.0 | 25.6±2.4 |
| 2281.9 | 8 | 19.7±1.9 | 9.8±1.8 | -2.8±2.1 | 17.3±2.0 | 25.9±2.4 |
| 2283.8 | -16 | 19.7±1.4 | 8.7±1.5 | -3.7±1.6 | 18.1±1.5 | 27.1±1.9 |
| 2285.2 | 9 | 19.0±1.7 | 8.4±1.7 | -3.8±1.8 | 17.4±1.7 | 26.3±2.2 |
| 2286.5 | 10 | 18.3±1.9 | 7.0±2.0 | -5.0±2.0 | 17.6±1.8 | 26.6±2.5 |

Perhaps the most important observation is that the coupling constants change as a basis cavity mode is tuned between the target vibrations. These trends have been captured with polynomial fitted lines which are the solid lines in Figure 5. The fitted trends for the most positive branches are $W^+$ for vibration-vibration coupling, the $V_{1a}^+$ and $V_{1b}^+$ branches of the $V_1$ coupling of cavity and vibration at 2253 cm$^{-1}$, and the $V_{2b}^+$ and $V_{2b}^-$ branches of the $V_2$ coupling of cavity and vibration at 2293 cm$^{-1}$:

$$W^+ = (18.69 \pm 0.22\ cm^{-1}) + (0.256 \pm 0.010)(\tilde{\nu}_m - 2253\ cm^{-1}) \quad , \quad (4)$$

$$V_{1a}^+ = (22.52 \pm 0.09\ cm^{-1}) - (0.00278 \pm 0.0002812\ cm)(\tilde{\nu}_m - 2250\ cm^{-1})^2\ , \quad (5)$$

$$V_{1b}^+ = (19.88 \pm 0.16\ cm^{-1}) - (0.00745 \pm 0.00015\ cm)(\tilde{\nu}_m - 2245\ cm^{-1})^2\ , \quad (6)$$

$$V_{2a}^+ = (17.75 \pm 0.11)cm^{-1} - (0.00415 \pm 0.00017\ cm)(\tilde{\nu}_m - 2293\ cm^{-1}\ )^2, \quad (7)$$

$$V_{2b}^+ = (5.86 \pm 0.24)cm^{-1} - (0.291 \pm 0.011)(\tilde{\nu}_m - 2253\ cm^{-1}\ ), \quad (8)$$

with root mean square errors varying from 0.30 to 0.87 cm$^{-1}$ as the primary etalon cavity mode, $\tilde{\nu}_m$, is tuned from $2252.9\ to\ 2293.0\ cm^{-1}$. Notice that one can obtain the $V_{2b}^-$ branch of Figure 5 from $-V_{2b}^+$ above. So, the angle-tuned etalon is changing the cavity-vibration and vibration-vibration couplings.

**Table 3.** Percent contribution of vibrations and fringes (cavity modes) to mixed states by Hopfield coefficients for data at $\theta = 0^0$.

| Mixed State (cm$^{-1}$) | Fringes % | Vib 1 % | Vib 2 % |
|---|---|---|---|
| 2055 | 98.8 | 1.2 | 0.0 |
| 2128 | 97.0 | 2.9 | 0.0 |
| 2194 | 85.9 | 13.4 | 7.1 |
| 2237 | 36.7 | 52.4 | 11.0 |
| 2280 | 73.8 | 4.4 | 21.8 |
| 2304 | 16.3 | 18.3 | 65.4 |
| 2355 | 94.0 | 1.5 | 1.0 |
| 2427 | 98.4 | 1.5 | 0.1 |
| 2498 | 99.2 | 0.8 | 0.0 |

**3.5 Characterizing the Cavity-Vibration Mixtures.** The eigenvectors of the interaction Hamiltonian can be used to access the size of the contributions of vibration 1 ($\upsilon_2$ $C \equiv N$ stretch dominated post-Fermi vibration at 2253 cm$^{-1}$), vibration 2 ($\upsilon_{3+4}$ combination band dominated post-Fermi vibration at 2293 cm$^{-1}$), and the cavity modes (fringes). The modulus squared of the eigenvectors are Hopfield coefficients[3] or probabilities which were summed over the seven basis fringes to give a total fringe contribution to each mixed state, which is then compared to the squared eigenvector coefficients due to each vibration. The results at $\theta = 0^0$ are plotted in Figure 7 and given in Table 3. The basis states before interaction are given on the outside of Figure 7 and the resulting mixed states are given in the middle. The mixed states at the bottom and top have summed cavity mode contributions of 99.2% and 98.8%, respectively, correlating with the smallest cavity mode shifts of 2.8 cm$^{-1}$ and 2.4 cm$^{-1}$ seen in the Figure 4 simulations.

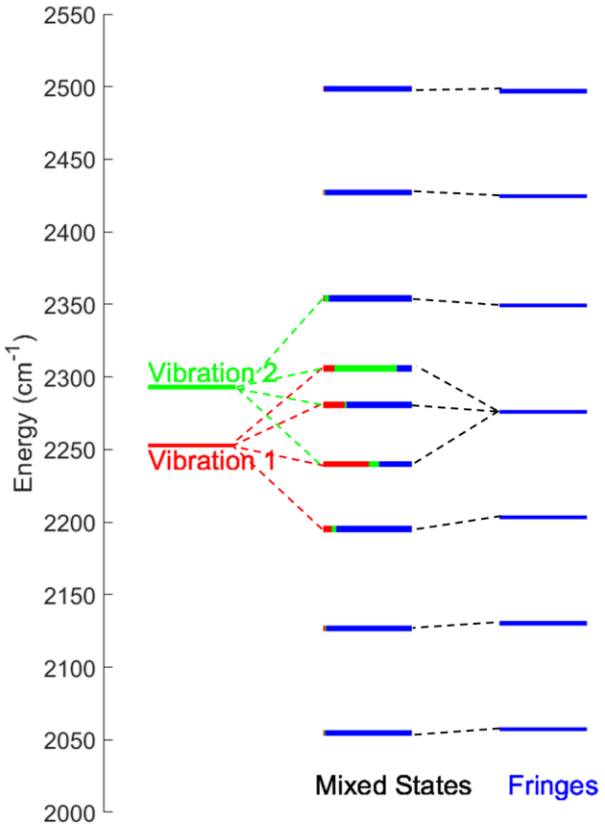


Figure 7. Energy level diagram of the basis states, vibrational states (left) and the cavity or fringe states (right) at the cavity tilt angle of $\theta$=0°, which interact to produce mixed states in the middle. Hopfield coefficients (eigenvector coefficients) have been used to determine the fractional contributions of vibration 1 (red), vibration 2 (green), and the fringes (blue) as coloring on the bar of each mixed state. While all basis states contribute to the mixed state results, the most important interactions have been indicated with dotted lines.

The mixed states second from bottom and top have summed cavity mode contributions of 97.0% and 98.4% correlating with the next smallest cavity mode shifts of 3.9 $cm^{-1}$ and 4.3 $cm^{-1}$ in Figure 4. Likewise, the mixed states third from the bottom and top have summed cavity mode contributions of 85.9% and 94.0%, respectively correlating with shifts of 8.7 $cm^{-1}$ and 6.6 $cm^{-1}$ in the Figure 4 simulation. The outer six mixed states relative to the primary interaction are dominated by basis cavity mode contributions (all above 85%) and are observed as having the highest transmissions in Figure 2. Interaction strengths can be gauged by the shifts of these peaks when the target vibrations are removed (Figure 4). The most highly mixed states are the middle three in Figure 2. They have the smallest transmissions and the highest vibrational character. They have interesting variations which depend on the interplay between the strengths of the vibrations and energetic spacings between the vibrations and the basis cavity mode states which vary with angle. Vibration 1 ($A_{15} = 5.771x10^{-4}$) is stronger than vibration 2 ($A_{16} = 1.886x10^{-4}$) and its effect can be seen as a fraction of the mixed state bar in Figure 7 with red for vibration 1. The nature of the mixtures can be varied with angle tuning. The mixed state observed at 2237 $cm^{-1}$ with $\theta = 0^0$ has the highest contribution of $C \equiv N$ stretch fundamental dominated vibration and the mixed state at 2304 $cm^{-1}$ has the highest contribution from the $\upsilon_{3+4}$ combination band dominated vibration.

**3.6 Dependence of Fit on Model Hamiltonian Parameters.**

The strong coupling regime is defined in practice in terms of the cavity state width and vibrational width relative to the observed energy splitting, but the current situation is more complicated involving multiple cavity modes and two vibrations of different isolated intensities. Specifically, the half-width-at-half-max (HWHM) of the vibrations are about 5 $cm^{-1}$, while the basis cavity mode HWHM are about 10 $cm^{-1}$. The sum of the HWHM is small compared to the

splitting expected for the strong target vibration ($2V_1$~ 48 cm$^{-1}$), however coupled vibrations are involved and so the effect of widths on these coupling results was tested. A complex Hamiltonian formalism[4, 78-82] subtracts $\gamma$, the HWHM of the basis functions, as an imaginary contribution to the diagonal elements of the interaction Hamiltonian of Equation 2. For example, the diagonal element of the primary fringe, $\tilde{\nu}_m$, in Equation 2, can be changed to $\tilde{\nu}_m - i\gamma_m$. Such a formalism allows one to fit both the spectral positions and widths of the mixed states, however the spectral widths of the cavity mode basis functions (before interaction) are not measured. Furthermore, the basis widths of the cavity modes in this analysis are not constant and increase with increasing wavenumber[56] and vary with the effects of nearby strong vibrations. As a test, but not an experimental result, the basis cavity mode widths were obtained by fitting the TM simulation fringes (blue trace in Figure 4) to Lorentzians and then multiplying all by a constant value (1.67 at $\theta = 0^0$) such that the outermost fringes, $\tilde{\nu}_{m-3}$ and $\tilde{\nu}_{m+3}$, which are the least affected by target vibrations, match the experimental measurements. As an example at $\theta = 0^0$, HWHM values of 8.67, 8.79, 9.10, 9.48, 10.56, 14.48, and 11.47 cm$^{-1}$ were used for $\tilde{\gamma}_{m-3}, \tilde{\gamma}_{m-2}, \ldots \tilde{\gamma}_{m+3}$, respectively, and HWHM of the vibrations were obtained from Table 2 and had values of $\tilde{\gamma}_{vib1} = 8.37/2 = 4.19\ cm^{-1}$ and $\tilde{\gamma}_{vib2} = 12.45/2 = 6.23\ cm^{-1}$. Using this complex formalism, the real part of the complex eigenvalues are the mixed state energies (in wavenumbers) and the imaginary part of the complex eigenvalues are the HWHMs. Table 4

**Table 4.** Coupling Constants at $\theta = 0^0$ with and without widths in the Hamiltonian of Equation 2.

| **Method** | $V_{1a}^+$ (cm$^{-1}$) | $V_{1b}^+$ (cm$^{-1}$) | $V_{2b}^+$ (cm$^{-1}$) | $V_{2a}^+$ (cm$^{-1}$) | $W^+$ (cm$^{-1}$) | $\sigma$ (cm$^{-1}$) |
|---|---|---|---|---|---|---|
| No Widths | 20.3±1.8 | 12.4±1.7 | -0.7±2.4 | 16.1±2.2 | 24.3±2.3 | 1.73 |
| Widths | 20.5±1.5 | 12.3±1.4 | -1.1±1.9 | 16.4±1.8 | 24.2±1.9 | 1.57 |

shows the results with and without widths at $\theta = 0^0$. Widths are not affecting the values of the coupling constants in this 9x9 Hamiltonian analysis outside of the error ranges. Future work might look for ways to measure cavity mode widths in the absence of vibrational interaction.

The question arises as to how many basis cavity modes are needed to get accurate coupling constants when there is nonzero vibrational-vibrational coupling? The issue was addressed by using a sequence of fewer cavity modes as basis functions, namely 7, 5, 3, and 1 cavity modes giving rise to Hamiltonians of 9x9, 7x7, 5x5, and 3x3 size. The results are shown in Table 5. The use of a 3x3 internal Hamiltonian, which only includes the primary interaction of one cavity mode and two target vibrations, gives values of $W$ which are not constant and ~60% too low as well as many other problems. Clearly better answers are obtained as more basis cavity modes are used.

**Table 5.** Coupling Constants at $\theta = 0^0$ using different numbers of basis set cavity modes. Note that the 3x3 method allows no errors to be determined.

| **Method** | $V_{1a}^{+}$ (cm$^{-1}$) | $V_{1b}^{+}$ (cm$^{-1}$) | $V_{2b}^{+}$ (cm$^{-1}$) | $V_{2a}^{+}$ (cm$^{-1}$) | $W^{+}$ (cm$^{-1}$) | $\sigma$ (cm$^{-1}$) |
|---|---|---|---|---|---|---|
| 9x9 | 20.3±1.8 | 12.4±1.7 | -0.7±2.4 | 16.1±2.3 | 24.3±2.3 | 1.73 |
| 7x7 | 20.4±2.1 | 12.5±1.9 | -0.8±2.7 | 16.1±2.5 | 23.9±2.7 | 1.99 |
| 5x5 | 20.6±2.4 | 12.7±2.1 | -1.1±3.0 | 16.2±2.8 | 22.9±3.2 | 2.25 |
| 3x3* | 22.7 | 14.9 | 5.5 | 16.9 | 13.6<br>14.9 | |

*3 parameters from three points, no statistics, absolute values of parameters

## 4 Conclusions

The most important result of this work was the change of the Fermi vibration-vibration coupling ($W^{+}$) between the $\upsilon_2$ $C \equiv N$ stretch dominated vibration and the $\upsilon_{3+4}$ combination band dominated vibration of liquid acetonitrile. It changed from $18.7 \pm 0.2$ to $28.9 \pm 0.5$ $cm^{-1}$ as a cavity mode was tuned from 2252.9 to 2293.0 $cm^{-1}$ - which passes through the value outside of a cavity estimated as 19.6 cm$^{-1}$. Clearly, Fermi interaction vibrational coupling can be changed upon interaction with the cavity mode of an etalon. Likewise, the cavity-vibration couplings also

change in interesting ways. The $V_{1a}^{+}$ and $V_{2a}^{+}$ branches are separated by 11 cm$^{-1}$ when the primary fringe is near the $\upsilon_2$ $C \equiv N$ stretch dominated vibration and these branches merge when the primary fringe is near the the $\upsilon_{3+4}$ combination band dominated vibration. Similarly, the $V_{1b}^{+}$ and $V_{2b}^{-}$ branches are separated by 26 cm$^{-1}$ when the primary fringe is near the $\upsilon_2$ $C \equiv N$ stretch dominated vibration and these branches merge when the primary fringe is near the $\upsilon_{3+4}$ combination band dominated vibration. Considering that different solvents[52-53] or metal cations[54] can change the target vibration frequencies by changing Fermi interactions, it is a very interesting possibility that angle-tuning of the cavity etalon mode causes changes in the $V_1$ and $V_2$ cavity-vibration coupling parameters modulating the strength of the Fermi resonance between target vibrations.

The Hopfield coefficients in Table 3 show that the 6 cavity-dominated, mixed states have vibrational contributions varying from 0 to 16% which are also detectable as shifts from the predicted fringe positions without the target vibrations. The cavity-dominated mixed states corresponding to $\tilde{\nu}_{m-3}$ and $\tilde{\nu}_{m+3}$ at the edge of the working spectral range were shifted by ~3 cm$^{-1}$ at an energetic spacing of more than 220 cm$^{-1}$ as was detectable with both the TM method simulation and the 9x9 interaction Hamiltonian. This is an impressive effect over such a large energetic spacing. While the ~56 μm etalon spacer gives a good match between the widths of cavity modes and liquid acetonitrile target vibrations, it also produces a small free spectral range which places more cavity modes within range of the target vibrations. A material without vibrations has a constant index of refraction which will have a constant spacing of cavity modes. In this work, the spacing between adjacent cavity modes was ~73 $cm^{-1}$, however the observed spacings of etalon dominated mixed states are not constant and are strongly perturbed by the target vibrations. The same physics that has each and every cavity mode interacting with the

vibrations gives rise to the well-known change of complex index of refraction with wavelength, as well as the need to have $V_1$ and $V_2$ interacting with each and every cavity mode in the interaction Hamiltonian model. While the 3x3 internal Hamiltonian of one cavity mode and two vibrations contains the primary interactions, a 9x9 internal Hamiltonian (7 cavity modes interacting with two vibrations) was needed to extract constant values of the coupling parameters. There is an analogy with using bigger basis sets in ab initio calculations. The narrowness of the cavity modes with a 56 μm etalon spacer came with the price of requiring more basis cavity modes in the analysis, but allowed the study of Fermi interaction by vibrational-vibrational coupling within an etalon.

**Acknowledgements**

We gratefully acknowledge the National Science Foundation for support of this work under grant number CHE 1800414.

**References**

(1) Lather, J.; Bhatt, P.; Thomas, A.; Ebbesen, T. W.; George, J., Cavity Catalysis by Cooperative Vibrational Strong Coupling of Reactant and Solvent Molecules. *Angew. Chem., Int. Ed.* **2019,** *58* (31), 10635-10638.

(2) Hertzog, M.; Boerjesson, K., The Effect of Coupling Mode in the Vibrational Strong Coupling Regime. *ChemPhotoChem* **2020,** *4* (8), 612-617.

(3) Hertzog, M.; Wang, M.; Mony, J.; Boerjesson, K., Strong light-matter interactions: a new direction within chemistry. *Chem. Soc. Rev.* **2019,** *48* (3), 937-961.

(4) Felipe Herrera; Owrutsky, J., Molecular polaritons for controlling chemistry with quantum optics. *J. Chem. Phys.* **2020,** *152* (10), 100902.

(5) Xiang, B.; Ribeiro, R. F.; Dunkelberger, A. D.; Wang, J.; Li, Y.; Simpkins, B. S.; Owrutsky, J. C.; Yuen-Zhou, J.; Xiong, W., Two-dimensional infrared spectroscopy of vibrational polaritons. *Proc. Natl. Acad. Sci. U. S. A.* **2018,** *115* (19), 4845-4850.

(6) Torma, P.; Barnes, W. L., Strong coupling between surface plasmon polaritons and emitters: a review. *Rep. Prog. Phys.* **2015,** *75*, 013901/1-013901/34.

(7) Khitrova, G.; Gibbs, H. M.; Kira, M.; Koch, S. W.; Scherer, A., Vacuum Rabi splitting in semiconductors. *Nat. Phys.* **2006,** *2* (2), 81-90.

(8) Flick, J.; Narang, P., Cavity-Correlated Electron-Nuclear Dynamics from First Principles. *Phys. Rev. Lett.* **2018,** *121* (11), 113002.

(9) Flick, J.; Rivera, N.; Narang, P., Strong light-matter coupling in quantum chemistry and quantum photonics. *Nanophotonics* **2018,** *7* (9), 1479-1501.

(10) Hutchison, J. A.; Schwartz, T.; Genet, C.; Devaux, E.; Ebbesen, T. W., Modifying Chemical Landscapes by Coupling to Vacuum Fields. *Angew. Chem.-Int. Edit.* **2012,** *51* (7), 1592-1596.

(11) Raimond, J. M.; Haroche, S., Atoms in cavities. *NATO ASI Ser., Ser. B* **1995,** *340* (Confined Electrons and Photons), 383-426.

(12) Haroche, S.; Raimond, J.-M., *Exploring the Quantum: Atoms, Cavities, aaand Photons*. Oxford: 2013; p 616.

(13) Long, J. P.; Simpkins, B. S., Coherent Coupling between a Molecular Vibration and Fabry-Perot Optical Cavity to Give Hybridized States in the Strong Coupling Limit. *ACS Photonics* **2015,** *2* (1), 130-136.

(14) Simpkins, B. S.; Fears, K. P.; Dressick, W. J.; Spann, B. T.; Dunkelberger, A. D.; Owrutsky, J. C., Spanning Strong to Weak Normal Mode Coupling between Vibrational and

Fabry-Perot Cavity Modes through Tuning of Vibrational Absorption Strength. *ACS Photonics* **2015,** *2* (10), 1460-1467.

(15) Shalabney, A.; George, J.; Hutchison, J.; Pupillo, G.; Genet, C.; Ebbesen, T. W., Coherent coupling of molecular resonators with a microcavity mode. *Nat. Commun.* **2015,** *6*, 5981.

(16) George, J.; Shalabney, A.; Hutchison, J. A.; Genet, C.; Ebbesen, T. W., Liquid-Phase Vibrational Strong Coupling. *J. Phys. Chem. Lett.* **2015,** *6* (6), 1027-1031.

(17) Ebbesen, T. W., Hybrid Light-Matter States in a Molecular and Material Science Perspective. *Acc. Chem. Res.* **2016,** *49* (11), 2403-2412.

(18) Dunkelberger, A. D.; Grafton, A. B.; Vurgaftman, I.; Soykal, O. O.; Reinecke, T. L.; Davidson, R. B.; Simpkins, B. S.; Owrutsky, J. C., Saturable Absorption in Solution-Phase and Cavity-Coupled Tungsten Hexacarbonyl. *ACS Photonics* **2019,** *6* (11), 2719-2725.

(19) Dunkelberger, A. D.; Davidson Ii, R. B.; Ahn, W.; Simpkins, B. S.; Owrutsky, J. C., Ultrafast Transmission Modulation and Recovery via Vibrational Strong Coupling. *J. Phys. Chem. A* **2018,** *122* (4), 965-971.

(20) Ahn, W.; Vurgaftman, I.; Dunkelberger, A. D.; Owrutsky, J. C.; Simpkins, B. S., Vibrational Strong Coupling Controlled by Spatial Distribution of Molecules within the Optical Cavity. *ACS Photonics* **2018,** *5* (1), 158-166.

(21) Ahn, W.; Vurgaftman, I.; Dunkelberger, A. D.; Owrutsky, J. C.; Simpkins, B. S., Vibrational Strong Coupling Controlled by Spatial Distribution of Molecules within the Optical Cavity. *ACS Photonics* **2017**.

(22) Thomas, A.; George, J.; Shalabney, A.; Dryzhakov, M.; Varma, S. J.; Moran, J.; Chervy, T.; Zhong, X.; Devaux, E.; Genet, C.; Hutchison, J. A.; Ebbesen, T. W., Ground-State Chemical

Reactivity under Vibrational Coupling to the Vacuum Electromagnetic Field. *Angew. Chem. Int. Ed.* **2017,** *55*, 11462-11466.

(23) Vergauwe, R. M. A.; George, J.; Chervy, T.; Hutchison, J. A.; Shalabney, A.; Torbeev, V. Y.; Ebbesen, T. W., Quantum Strong Coupling with Protein Vibrational Modes. *J. Phys. Chem. Lett.* **2016,** *7* (20), 4159-4164.

(24) Thomas, A.; George, J.; Shalabney, A.; Dryzhakov, M.; Varma, S. J.; Moran, J.; Chervy, T.; Zhong, X.; Devaux, E.; Genet, C.; Hutchison, J. A.; Ebbesen, T. W., Ground-State Chemical Reactivity under Vibrational Coupling to the Vacuum Electromagnetic Field. *Angew. Chem., Int. Ed.* **2016,** *55* (38), 11462-11466.

(25) George, J.; Chervy, T.; Shalabney, A.; Devaux, E.; Hiura, H.; Genet, C.; Ebbesen, T. W., Multiple Rabi splittings under ultrastrong vibrational coupling. *Phys. Rev. Lett.* **2016,** *117* (15), 153601/1-153601/5.

(26) Crum, V. F.; Casey, S. R.; Sparks, J. R., Photon-mediated hybridization of molecular vibrational states. *Phys. Chem. Chem. Phys.* **2018,** *20* (2), 850-857.

(27) Imran, I.; Nicolai, G. E.; Stavinski, N. D.; Sparks, J. R., Tuning Vibrational Strong Coupling with co-Resonators. *ACS Photonics* **2019,** *6* (10), 2405-2412.

(28) Casey, S. R.; Sparks, J. R., Vibrational Strong Coupling of Organometallic Complexes. *J. Phys. Chem. C* **2016,** *120* (49), 28138-28143.

(29) Muallem, M.; Palatnik, A.; Nessim, G. D.; Tischler, Y. R., Strong Light-Matter Coupling and Hybridization of Molecular Vibrations in a Low-Loss Infrared Microcavity. *J. Phys. Chem. Lett.* **2016,** *7* (11), 2002-2008.

(30) Muallem, M.; Palatnik, A.; Nessim, G. D.; Tischler, Y. R., Strong light-matter coupling between a molecular vibrational mode in a PMMA film and a low-loss mid-IR microcavity. *Ann. Phys. (Berlin, Ger.)* **2016,** *528* (3-4), 313-320.

(31) Kapon, O.; Yitzhari, R.; Palatnik, A.; Tischler, Y. R., Vibrational Strong Light-Matter Coupling Using a Wavelength-Tunable Mid-infrared Open Microcavity. *J. Phys. Chem. C* **2017,** *121* (34), 18845-18853.

(32) Justin D. Erwin; Madeline Smotzer; Coe, J. V., Effect of Strongly Coupled Vibration–Cavity Polaritons on the Bulk Vibrational States within a Wavelength-Scale Cavity. *J. Phys. Chem . B* **2019**.

(33) Chervy, T.; Thomas, A.; Akiki, E.; Vergauwe, R. M. A.; Shalabney, A.; George, J.; Devaux, E.; Hutchison, J. A.; Genet, C.; Ebbesen, T. W., Vibro-Polaritonic IR Emission in the Strong Coupling Regime. *ACS Photonics* **2018,** *5* (1), 217-224.

(34) Kapon, O.; Yitzhari, R.; Palatnik, A.; Tischler, Y. R., Vibrational Strong Light–Matter Coupling Using a Wavelength-Tunable Mid-infrared Open Microcavity. *The Journal of Physical Chemistry C* **2017,** *121* (34), 18845-18853.

(35) Dunkelberger, A. D.; Davidson, R. B.; Ahn, W.; Simpkins, B. S.; Owrutsky, J. C., Ultrafast Transmission Modulation and Recovery via Vibrational Strong Coupling. *The Journal of Physical Chemistry A* **2018,** *122* (4), 965-971.

(36) Xiang, B.; Ribeiro, R. F.; Dunkelberger, A. D.; Wang, J.; Li, Y.; Simpkins, B. S.; Owrutsky, J. C.; Yuen-Zhou, J.; Xiong, W., Two-dimensional infrared spectroscopy of vibrational polaritons. *Proceedings of the National Academy of Sciences* **2018,** *115* (19), 4845.

(37) Thomas, A.; Lethuillier-Karl, L.; Nagarajan, K.; Vergauwe, R. M. A.; George, J.; Chervy, T.; Shalabney, A.; Devaux, E.; Genet, C.; Moran, J.; Ebbesen, T. W., Tilting a ground-state reactivity landscape by vibrational strong coupling. *Science* **2019,** *363* (6427), 615.

(38) Muallem, M.; Palatnik, A.; Nessim, G. D.; Tischler, Y. R., Strong Light-Matter Coupling and Hybridization of Molecular Vibrations in a Low-Loss Infrared Microcavity. *The Journal of Physical Chemistry Letters* **2016,** *7* (11), 2002-2008.

(39) Strashko, A.; Keeling, J., Raman scattering with strongly coupled vibron-polaritons. *Phys. Rev. A* **2016,** *94* (2), 023843.

(40) Vergauwe, R. M. A.; George, J.; Chervy, T.; Hutchison, J. A.; Shalabney, A.; Torbeev, V. Y.; Ebbesen, T. W., Quantum Strong Coupling with Protein Vibrational Modes. *The Journal of Physical Chemistry Letters* **2016,** *7* (20), 4159-4164.

(41) George, J.; Chervy, T.; Shalabney, A.; Devaux, E.; Hiura, H.; Genet, C.; Ebbesen, T. W., Multiple Rabi Splittings under Ultrastrong Vibrational Coupling. *Phys. Rev. Lett.* **2016,** *117* (15), 153601.

(42) Hernández, F. J.; Herrera, F., Multi-level quantum Rabi model for anharmonic vibrational polaritons. *The Journal of Chemical Physics* **2019,** *151* (14), 144116.

(43) Shalabney, A.; George, J.; Hiura, H.; Hutchison, J. A.; Genet, C.; Hellwig, P.; Ebbesen, T. W., Enhanced Raman Scattering from Vibro-Polariton Hybrid States. *Angewandte Chemie (International ed. in English)* **2015,** *54* (27), 7971-7975.

(44) Long, J. P.; Simpkins, B. S., Coherent Coupling between a Molecular Vibration and Fabry–Perot Optical Cavity to Give Hybridized States in the Strong Coupling Limit. *ACS Photonics* **2015,** *2* (1), 130-136.

(45) Lather, J.; Bhatt, P.; Thomas, A.; Ebbesen, T. W.; George, J., Cavity Catalysis by Cooperative Vibrational Strong Coupling of Reactant and Solvent Molecules. *Angew. Chem. Int. Ed.* **2019,** *58* (31), 10635-10638.

(46) Thomas, A.; Jayachandran, A.; Lethuillier-Karl, L.; Vergauwe, R. M. A.; Nagarajan, K.; Devaux, E.; Genet, C.; Moran, J.; Ebbesen, T. W., Ground state chemistry under vibrational strong coupling: dependence of thermodynamic parameters on the Rabi splitting energy. *Nanophotonics* **2020,** *9* (2), 249-255.

(47) Pang, Y.; Thomas, A.; Nagarajan, K.; Vergauwe, R. M. A.; Joseph, K.; Patrahau, B.; Wang, K.; Genet, C.; Ebbesen, T. W., On the Role of Symmetry in Vibrational Strong Coupling: The Case of Charge-Transfer Complexation. *Angew. Chem., Int. Ed.* **2020,** *59* (26), 10436-10440.

(48) Vergauwe, R. M. A.; Thomas, A.; Nagarajan, K.; Shalabney, A.; George, J.; Chervy, T.; Seidel, M.; Devaux, E.; Torbeev, V.; Ebbesen, T. W., Modification of Enzyme Activity by Vibrational Strong Coupling of Water. *Angew. Chem., Int. Ed.* **2019,** *58* (43), 15324-15328.

(49) Seidel, M.; Chervy, T.; Thomas, A.; Akiki, E.; Vergauwe, R. M. A.; Shalabney, A.; George, J.; Devaux, E.; Hutchison, J. A.; Genet, C.; Ebbesen, T. W., Correction to Vibro-Polaritonic IR Emission in the Strong Coupling Regime. *ACS Photonics* **2019,** *6* (7), 1823-1825.

(50) Venkateswarlu, P., Rotation-vibration spectrum of methyl cyanide in the region 1.6 μ-20 μ. *J. Chem. Phys.* **1951,** *19*, 293-8.

(51) Herzberg, G., *Molecular Spectra and Molecular Structure: II. Infrared and Raman Spectra of Polyatomic Molecules*. Krieger: 1989.

(52) Fawcett, W. R.; Liu, G.; Kessler, T. E., Solvent-induced frequency shifts in the infrared spectrum of acetonitrile in organic solvents. *J. Phys. Chem.* **1993,** *97* (37), 9293-8.

(53) Reimers, J. R.; Hall, L. E., The Solvation of Acetonitrile. *J. Am. Chem. Soc.* **1999,** *121* (15), 3730-3744.

(54) Addison, C. C.; Amos, D. W.; Sutton, D., Infrared and Raman spectra of solutions of zinc, cadmium, and mercury(II) nitrates in acetonitrile. *J. Chem. Soc., A* **1968,** (9), 2285-90.

(55) Kwon, Y.; Lee, C.; Park, S., Effect of ion-molecule interaction on Fermi-resonance in acetonitrile studied by ultrafast vibrational spectroscopy. *Chem. Phys.* **2014,** *445*, 38-45.

(56) Coe, J. V.; Erwin, J. D.; Bradley, R. C. In *Reconstructing fringes for cavity-vibration experiments in FTIR spectrometers*, Proc.SPIE, 2019; pp 1091702-1 to 1091702-7.

(57) Coe, J. V., *Data Fitting and Error Analysis with MATLAB®: Things You Get from Physical Chemistry Lab, but Need in All of Science and Engineering*. Amazon Kindle Direct Publishing: 2018; p 65.

(58) Myers, T. L.; Tonkyn, R. G.; Danby, T. O.; Taubman, M. S.; Bernacki, B. E.; Birnbaum, J. C.; Sharpe, S. W.; Johnson, T. J., Accurate Measurement of the Optical Constants n and k for a Series of 57 Inorganic and Organic Liquids for Optical Modeling and Detection. *Appl. Spectrosc.* **2018,** *72* (4), 535-550.

(59) Luthra, A.; Ravi, A.; Li, S.; Nystrom, S. V.; Thompson, Z.; Coe, J. V., Dust library of plasmonically enhanced infrared spectra of individual respirable particles. *Appl. Spectrosc.* **2016,** *70* (9), 1546-1554.

(60) Bertie, J. E.; Zhang, S. L.; Eysel, H. H.; Baluja, S.; Ahmed, M. K., Infrared intensities of liquids. XI: infrared refractive indices from 8000 to 2 cm-1, absolute integrated intensities, and dipole moment derivatives of methanol at 25 °C. *Appl. Spectrosc.* **1993,** *47* (8), 1100-14.

(61) Bertie, J. E.; Zhang, S. L.; Dale Keefe, C., Measurement and use of absolute infrared absorption intensities of neat liquids. *Vib. Spectrosc.* **1995,** *8* (2), 215-30.

(62) Bertie, J. E.; Lan, Z., An accurate modified Kramers-Kronig transformation from reflectance to phase shift on attenuated total reflection. *J. Chem. Phys.* **1996,** *105* (19), 8502-8514.

(63) Bertie, J. E.; Lan, Z., Liquid Water-Acetonitrile Mixtures at 25 °C: The Hydrogen-Bonded Structure Studied through Infrared Absolute Integrated Absorption Intensities. *J. Phys. Chem. B* **1997,** *101* (20), 4111-4119.

(64) Lagarias, J. C.; Reeds, J. A.; Wright, M. H.; Wright, P. E., Convergence Properties of the Nelder--Mead Simplex Method in Low Dimensions. *SIAM Journal on Optimization* **1998,** *9* (1), 112-147.

(65) Nelder, J. A.; Mead, R., A simplex method for function minimization. *The Computer Journal* **1965,** *7* (4), 308–313.

(66) Nelder, J. A.; Mead, R., errata. *The Computer Journal* **1965,** *8* (1), 27.

(67) Fano, U., The Theory of Anomalous Diffraction Grating and of Quasi-Stationary Waves on Metallic Surfaces (Sommerfield's Waves). *J. Opt. Soc. Am.* **1941,** *31* (3), 213-222.

(68) Born, M.; Wolf, E., *principles of Optics*. 7th ed.; Cambridge University Press: 1999.

(69) Pascoe, K. J. *Reflectivity and Transmissivity through Layered, Lossy Media: A User-Friendly Approach*; Air Force Institute of Technology: Wrigth-Patterson Air Force Base, 2001.

(70) Rakic, A. D.; Djurisic, A. B.; Elazar, J. M.; Majewski, M. L., Optical properties of metallic films for vertical-cavity optoelectronic devices. *Appl. Opt.* **1998,** *37* (22), 5271-5283.

(71) Du, M.; Martínez-Martínez, L. A.; Ribeiro, R. F.; Hu, Z.; Menon, V. M.; Yuen-Zhou, J., Theory for polariton-assisted remote energy transfer. *Chemical Science* **2018,** *9* (32), 6659-6669.

(72) Du, M.; Ribeiro, R. F.; Yuen-Zhou, J., Remote Control of Chemistry in Optical Cavities. *Chem* **2019,** *5* (5), 1167-1181.

(73) F. Ribeiro, R.; Dunkelberger, A. D.; Xiang, B.; Xiong, W.; Simpkins, B. S.; Owrutsky, J. C.; Yuen-Zhou, J., Theory for Nonlinear Spectroscopy of Vibrational Polaritons. *The Journal of Physical Chemistry Letters* **2018,** *9* (13), 3766-3771.

(74) Flick, J.; Ruggenthaler, M.; Appel, H.; Rubio, A., Atoms and molecules in cavities, from weak to strong coupling in quantum-electrodynamics (QED) chemistry. *Proceedings of the National Academy of Sciences* **2017,** *114* (12), 3026.

(75) Pino, J. d.; Feist, J.; Garcia-Vidal, F. J., Quantum theory of collective strong coupling of molecular vibrations with a microcavity mode. *New Journal of Physics* **2015,** *17* (5), 053040.

(76) Craig, D. P.; Thirunamachandran, T., *Molecular Quantum Electrodynamics: An Introduction to Radiation Molecule Interactions*. Dover Publications, Inc.: Mineola, New York, 1984.

(77) Mandal, A.; Huo, P., Investigating New Reactivities Enabled by Polariton Photochemistry. *The Journal of Physical Chemistry Letters* **2019,** *10* (18), 5519-5529.

(78) Panzarini, G.; Andreani, L. C.; Armitage, A.; Baxter, D.; Skolnick, M. S.; Astratov, V. N.; Roberts, J. S.; Kavokin, A. V.; Vladimirova, M. R.; Kaliteevski, M. A., Exciton-light coupling in single and coupled semiconductor microcavities: Polariton dispersion and polarization splitting. *Phys. Rev. B: Condens. Matter Mater. Phys.* **1999,** *59* (7), 5082-5089.

(79) Savona, V.; Andreani, L. C.; Schwendimann, P.; Quattropani, A., Quantum well excitons in semiconductor microcavities: unified treatment of weak and strong coupling regimes. *Solid State Commun.* **1995,** *93* (9), 733-9.

(80) Nelson, T. R. J.; Lindmark, E. K.; Wick, D. V.; Tai, K.; Khitrova, G.; Gibbs, H. M., Normal-mode coupling in planar semiconductor microcavities. *NATO ASI Ser., Ser. E* **1996,** *324* (Microcavities and Photonic Bandgaps: Physics and Applications), 43-57.

(81) Ell, C.; Prineas, J.; Nelson, T. R.; Park, S.; Lee, E. S.; Gibbs, H. M.; Khitrova, G.; Koch, S. W., Excitonic features in semiconductor microcavities. *Advances in Laser Physics* **2000,** *1*, 67-83.

(82) Gibbs, H. M.; Khitrova, G.; Koch, S. W., Exciton-polariton light-semiconductor coupling effects. *Nat. Photonics* **2011,** *5* (5), 275-282.